Optimised dynamic line scan thermographic detection of CFRP inserts using FE updating and POD analysis

Reference:
Peeters Jeroen, Ibarra-Castanedo C., Khodayar F., Mokhtari Y., Sfarra S., Zhang H., Maldague X., Dirckx Joris, Steenackers Gunther.- Optimised dynamic line scan thermographic detection of CFRP inserts using FE updating and POD analysis
NDT and E international: the independant non-destructive testing and evaluation - ISSN 0963-8695 - 93(2018), p. 141-149
Full text (Publisher's DOI): https://doi.org/10.1016/J.NDTEINT.2017.10.006
To cite this reference: https://hdl.handle.net/10067/1466140151162165141

Optimised Dynamic line scan thermographic detection of CFRP inserts using FE updating and POD analysis

J. Peeters[a,*], C. Ibarra-Castanedo[b], F. Khodayar[b], Y. Mokhtari[b], S. Sfarra[c,d], H. Zhang[b], X. Maldague[b], J.J.J. Dirckx[f], G. Steenackers[a,e]

[a] *University of Antwerp, Op3Mech, Groenenborgerlaan 171, B-2020 Antwerp, Belgium. Tel.: +32-3-2051938*

[b] *Laval University, Computer Vision and Systems Laboratory, Electrical and Computer Engineering Department, 1065 av de la Medecine, Quebec, Canada, G1V 0A6.*

[c] *Las.E.R. Laboratory, Department of Industrial and Information Engineering and Economics (DIIIE), University of L'Aquila, Piazzale E. Pontieri 1, Loc. Monteluco di Roio, Roio Poggio, 67100 L'Aquila, AQ, Italy.*

[d] *Tomsk Polytechnic University, Lenin Av., 30, Tomsk 634050, Russia.*

[e] *Vrije Universiteit Brussel, Acoustics & Vibration Research Group, Pleinlaan 2, B-1050, Brussels, Belgium.*

[f] *University of Antwerp, Laboratory of Biomedical Physics, Groenenborgerlaan 171, B-2020 Antwerp, Belgium.*

Abstract

The detection of delaminations in composite laminates using automated thermographic scanning is a quite challenging task. The set-up parameters are not only dependent on the equipment, but on the inspected component as well. In this work, a methodology is discussed to use Finite Element (FE) model updating to automatically establish the most suitable inspection parameters for a given combination of the structure and the investigated delamination depths. The optimised results are compared using binary Probability of Detection analysis and are benchmarked with parameter sets retrieved by an expert using the regular trial & error approach. The results show an improvement of the accuracy and scanning speed which significantly increases as the POD decreases and the complexity of the samples increases.

Keywords: Dynamic line scan, FE updating, Inverse problem, automated NDT, Quantitative Non-destructive Evaluation, CFRP, Probability of Detection

*Ing. Jeroen Peeters

Email address: `jeroen.peeters2@uantwerpen.be` (J. Peeters)

URL: `www.op3mech.be` (J. Peeters)

1. Introduction

Active thermography is a broadly used technology to inspect large, carbon fibre reinforced plastic (CFRP) components for flaws in a fast way [1, 2, 3]. To receive accurate results on large samples, the thermal camera has to be repositioned over the structure in a way each surface is inspected with sufficient accuracy with an equal heat excitation and time resolution considering directional emissivity [4, 5, 6]. To perform these sequential experiments in a robust, repetitive way, NASA developed a type of line Scan thermography (LST) whereby a robotised movement is used to reposition both the heating device as the infrared thermal camera in tandem [6, 7, 8]. Those ideas are based on the ideas of Maldague in 1993 [9] and on the work of Lindberg in 1968. Lindberg proposed the idea of a prism line-scanner for high speed thermography, at that time mono-detectors were used so even though the camera was not moving the laser heated the surface point-by-point and a reconstruction was performed to recover a complete image of the inspected surface [10]. In recent research, for the heating device, a thin line radiative heater is used and the acquired image sequence is processed to result in a pseudo-static representation of the full surface over time, to evaluate the subsurface integrity [1, 6]. The NASA developed and patented technology of the 1990s, as described by Cramer et al. has since been used by more and more industrial branches for inspection of metallic and composite components [8, 11]. There exists a similar technique with analogue problems, called the thermal-photocopier for which this work delivers similar insights [12]. The main difference with LST is that the camera remains fixed and only the heat source is moving.

Automatic scanning using a robotic arm is seen as an interesting way for Non-destructive Testing (NDT) of large and complex shaped components [6]. The programming of the inspection path, speed, excitation power and acquisition rate is a difficult task which is highly dependent on the inspected sample geometry and material properties [6, 13]. This parameter optimisation is mostly done manually by a highly qualified inspector using experience and trial and error which is a time-consuming task for complex structures as the heat deposition and scanning speed should match the heat diffusion in the material [13]. Within this work, it is shown that using numerical model updating within the field of active thermography inspection can facilitate the set-up of the measurements by predicting the most ideal setup parameters. The optimised results are compared using a Probability Of Detection analysis to compare with the work flow by trial and error followed by a skilled inspector.

The use of Finite Element (FE) models is well integrated into the design of large structures, but in uttermost cases, the use of the FE models remains in the design stage. FE model updating can be used to optimise the complex parameter set of the LST set-up by correlating the numerical results with NDT data. These methods are widely used in modal vibration inspection [14, 15, 16], but their usage is limited in thermal optimisation problems [17, 18] due to the difficulties in estimating the diffusivity.

The optimisation of LST set-up parameters using FE model optimisation is similar to the FE model updating techniques as described by Marwala [19] for modal analysis. There are a few differences with the well-known FE model optimisation routines for shape or model performance optimisations due to the complex interdependency between the experimental limitations (e.g. the experimental setup), for example, the camera sensitivity and the heat distribution of the excitation source. This results in a different manner of defining the objective function and solver choice described in Section 2.3.1. Besides, an extreme non-linear behaviour of the response to limited parameter differences and the different mathematical definition of thermal modes with respect to modal modes [20] results in the need for an accurate investigation of those influences.

The accuracy and the efficiency of an NDT technique, are mostly evaluated by using a Probability Of Detection (POD) analysis to determine the acceptance of a certain technique or to compare two distinguished technologies [21]. Probability of Detection (POD) is a statistical method used to estimate the proportion of defects of a given size that can be detected by a particular technique. It requires a large amount of samples having defects ranging from non-detectable to minimum detectable sizes and larger. PoD is often used to evaluate the reliability of a particular NDE method (x-rays, ultrasounds, Eddy currents, thermography, etc.), or a processing technique (principal components, Fourier transform, etc.), to detect a certain type of flaw (cracks, delaminations, impact damage, corrosion loss, etc.), at a given depth (or depth range) either manually or automatically. It has been utilised for years to validate the performance and reliability of NDE techniques such as ultrasounds and Eddy current techniques. In the case of infrared thermography, only a few POD studies can be found in the literature [22, 23, 24, 25]. In this study, the number of targets (defects of different sizes and depths) is rather limited (25 per side, which gives a total amount of 50 defects to detect). Nevertheless, POD analysis in this work is performed in order to receive an objective comparison between the optimised detection results and the results received by an experienced LST inspector and a randomly chosen parameter set. The amount of literature related to POD analyses of active thermography and especially for LST techniques is limited [21]. Due to the importance of the parameter optimisation, the implementation of statistical methods for the evaluation of the accuracy of the experimental set-up is provided in this manuscript. To perform an accurate POD analysis, a great amount of defective samples are required, with known defects ranging from non-detectable to good detectable size/depth ratios (D/d), also called aspect ratios [21, 26]. In this work, the discrete hit/miss evaluation technique is used on the same test sample that was employed by Duan et al. to deliver comparable results [21].

2. Materials & Methods

2.1. Experimental set-up

The experimental inspections were performed on a CFRP sample, widely described in literature [27, 28], with a thickness of 2 mm with 25 Teflon square inserts with lateral sizes $D = 3, 5, 7, 10$ and 15 mm placed between each consecutive ply at different depths, varying of $0.2 < d < 1$ mm from the front side and $1 < d < 1.8$ mm from the rear side, and locations as shown in Fig. 1. The specimen is tested from both sides which result in a total of 50 inspected flaws with different aspect ratios varying from 3/1.8 to 15/0.2). The sample is built from 10 unidirectional prepreg carbon fibre plies consisting of Hexcel

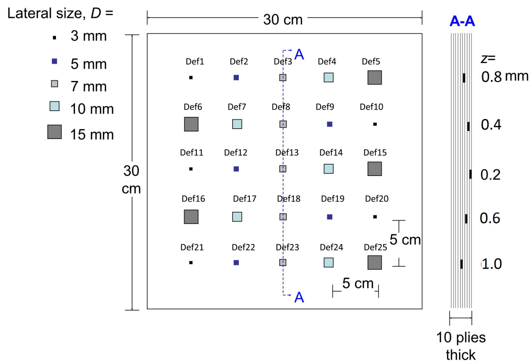

Figure 1: Technical drawing of the CFRP inserts.

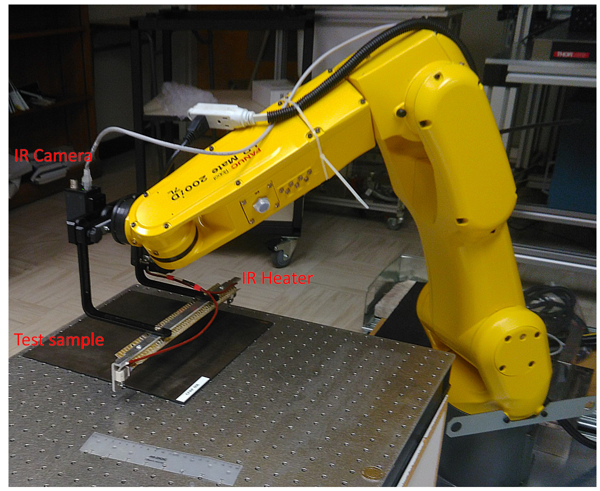

Figure 2: Experimental set-up of the dynamic line scan.

AS4/3501-6, 300 AW with 31% remaining resin after cure. The stacking within the sample follows a symmetric $[0\ 90]_{5 \cdot s}$ order. The test sample is fabricated using standard autoclave curing cycle. The sample is inspected using an inspection tool consisting of a FLIR A65sc microbolometric LWIR $7.5 - 14\mu m$ camera with a spatial resolution of 640x512 pixels for the data acquisition and an IR Heater of 30 cm with a total power of maximum 1500W as a heat source. The inspection tool is attached to a 6 degree of freedom FANUC LR Mate 200iD 7L robotic arm and makes use of consecutive linear scan paths starting from the same side of the sample. A photograph of the experimental set-up is shown in Fig. 2.

2.2. Numerical model description

The numerical model was developed using COMSOL Multiphysics 5.0 software based on the Finite Element technique. The model simulates the moving heat source of the LST set-up over the inspected test sample using multibody dynamics combined with heat transfer. The heat conductivity through the different material layers is simulated to implement the anisotropic behaviour of the lateral heat diffusion. A constant Newtonian non-linear method is used with a modernised implementation of the DAE solver within the heat transfer routine. This solver is based on the backwards differentiation formulas [29]. Linear tetrahedral Lagrange elements are used to simulate the behaviour of the material on the moving thermal heat source. The model consists of 41 406 elements with an average growth rate of 2.2 and an average element quality of 0.565. The model consists of a stacking of different layers for each CFRP ply with thermal anisotropic properties dependent on the fibre orientation of the ply. The different layer properties are estimated using a model where each ply consist of uniform carbon fibres with only one longitudinal conductivity and one different transversal in-plane conductivity. Between each ply, a thin epoxy layer is modelled to simulate the practical, not ideal contact layer between each carbon ply with the third variable conductivity coefficient, perpendicular to the plies. With this stacking

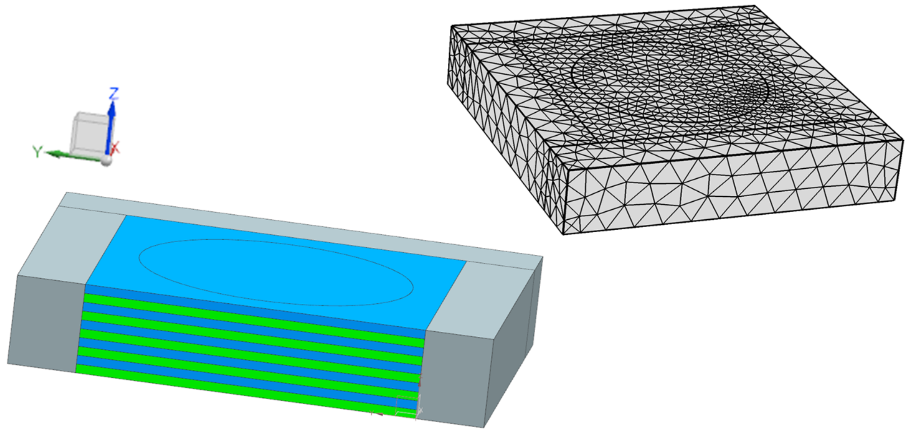

Figure 3: Overview of a subsection of the 3D mesh on the test sample with the different plies schematically represented by different colors.

recipient a quasi-isotropic laminate is represented. A detailed picture of the 3D mesh with the different layers is shown in Figure 3.

- 5 CFRP layer of 0.25mm thick with a global fibre orientation of $0°C$, in figure in blue represented.
- 5 CFRP layer of 0.25mm thick with a global fibre orientation of $90°C$, in figure in green represented.

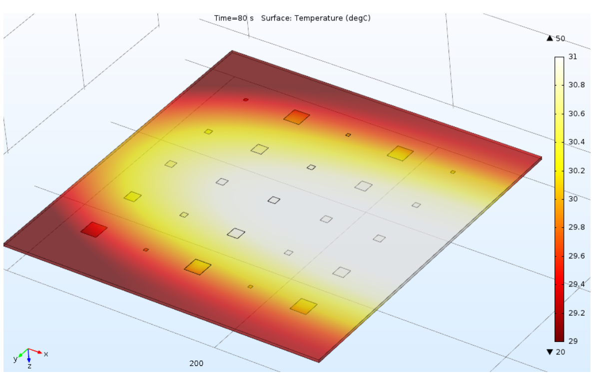

Figure 4: Simulation result of the optimised numerical model (scale in degC).

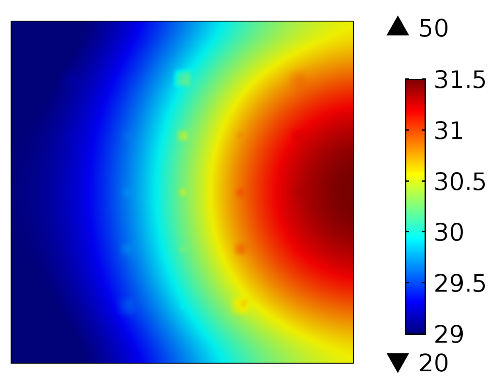

Figure 5: Spatial simulation result during LST simulation where the detection of the defects on different depths is visualised.

The essence of mesh convergence is acknowledged within this research and might result in significant errors within the updating routine. The computed model within this manuscript is checked on mesh convergence with a minimum acceptance rate of 95% accuracy on temperature level when the mesh is changed. It is found that the elements can be made rather large within this constraint for thermal simulations. The geometrical complexity by simulating the thin teflon inserts force the use of a smaller mesh which is more robust with respect to mesh convergence due to the minimal element quality needed in the area close to the simulated defects. A representation of the performed mesh convergence is shown with respect to temperature on a probe point on a certain time stamp in Figure 6. A red asterisk shows the used mesh within the optimisation routine.

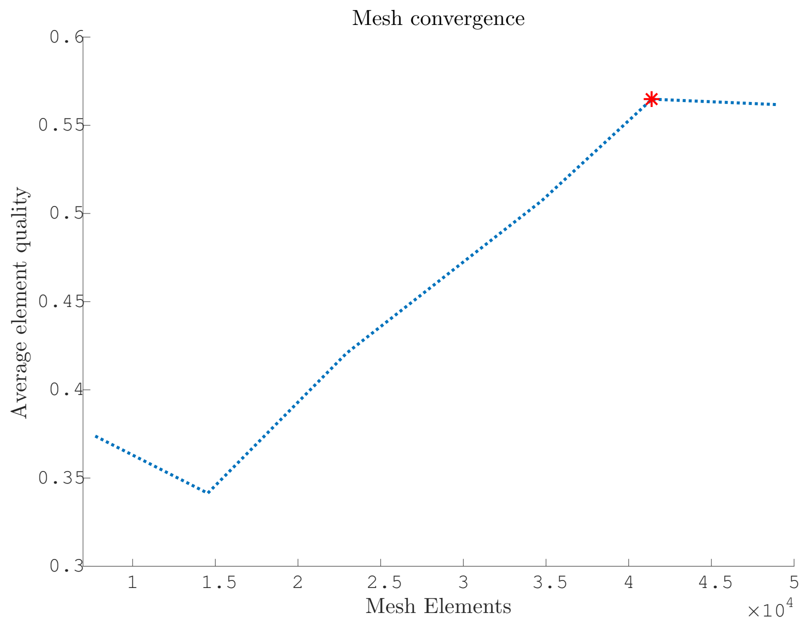

Figure 6: Mesh convergence analysis on 3D mesh.

2.2.1. Modelling of the excitation source

The tubular carbon excitation source results in a non homogeneous spatial distributed heat excitation which is shown in Figure 7. This spatial distribution is implemented in the excitation source modelling to correlate the spatial heat distribution on the inspected test sample according to the distribution in the X-axis. The narrow distribution in the Y-axis is transposed to the temporal distribution due to the lateral movement of the heat source. The movement of the heat source is simulated using a moving mesh for the radiating heat source with a horizontal speed perpendicular to the inspected surface which is equal to the robot speed around the global world coordinate system. The world coordinate system itself is placed similarly in the numerical model as for the robot used in the experimental measurements.

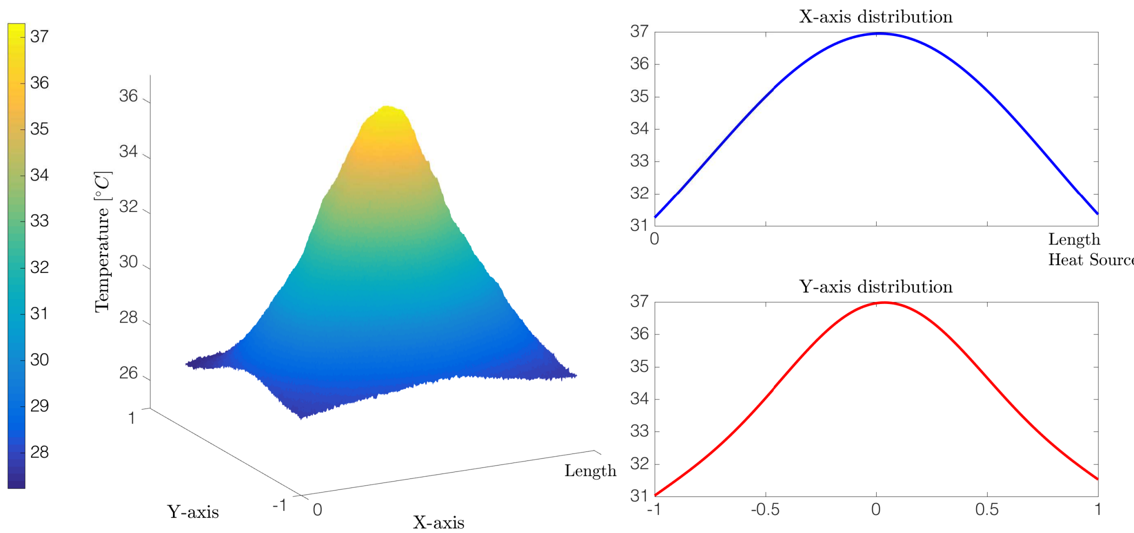

Figure 7: Spatial temperature distribution of the heat source.

2.2.2. Physical boundary conditions

For the heat transfer module in the simulation model, it is important to implement surface to surface radiance between the moving heat source and the upper surface of the test sample. Besides the radiative energy exchange between the heat source and the sample, the cooling mechanisms: convection and ambient radiation were also taken into account. A representation of the overall numerical model is shown in Figure 4 that corresponds to the time when the heat source has moved for 80 seconds and already passed the inspected plane.

The governing differential equation is a combined heat transfer equation with conduction, convective cooling and radiation of an external heat source, formulated in Eq.(1), Eq.(2) and Eq.(3) where ρ is the density, C_p is the heat capacity at constant pressure, T is the absolute surface temperature, κ is the thermal conductivity, t is the time, $Q(t)$ is the time dependent heat source, h is the coefficient of convection and σ is the constant of Stefan-Boltzmann [30, 31].

$$\rho C_p \frac{\partial T}{\partial t} + \nabla \cdot (-\kappa \nabla T) = Q \; with \; T\,(x, y, z, 0) = T_\infty = 292.88[K] \tag{1}$$

$$\vec{n}(k\nabla T) = h(T_\infty - T) \tag{2}$$

$$\vec{n}(k\nabla T) = \varepsilon \cdot \sigma \cdot (T_\infty^4 - T^4) \tag{3}$$

A few assumptions are made:

- The air velocity is assumed to be zero allowed by the laboratory conditions.
- The lay-up of the CFRP laminate is considered quasi-isotropic with structured fibre angles in a woven pattern.

Table 1: Material properties within the numerical model [32, 33, 34].

Parameter	Conductivity $k_{long}(W/m \cdot K)$	Conductivity $k_{trans}(W/m \cdot K)$	Specific heat capacity CFRP $C_p[J/(Kg.K)]$	Density CFRP $\rho[kg/m^3]$	Heat transfer coefficient $W/(m^2.K)$	Emissivity
Carbon	60	4.2	1000	1580	10	0.85
Teflon	0.265	0.265	950	2175	10	0.92

- The test sample is opaque and behaves like an ideal grey body as a result of the mate epoxy surface.

The physical properties used in the numerical model are shown in Table 1.

The accuracy of the material properties within the used test sample is validated within previous work on the test sample as provided in [35]. Using a similar optimisation routine, the material properties of the test sample are estimated with respect to the known simulated defect depths, represented by the teflon inserts. Therefore the inspection is validated with a standard pulsed thermography inspection. The accuracy of prediction of the defect depths is related to the accuracy of modelling the thermal diffusivity α in the test sample which gives a clear indication on the uncertainty of the used material properties. This is shown in Figure 8 where the importance of precise material properties within the numerical model is provided. The numerical model using standard material properties delivers the worst estimation of defect depths, especially when the defect depth increases. Due to the optimisation of the material properties, the accuracy is significantly increased.

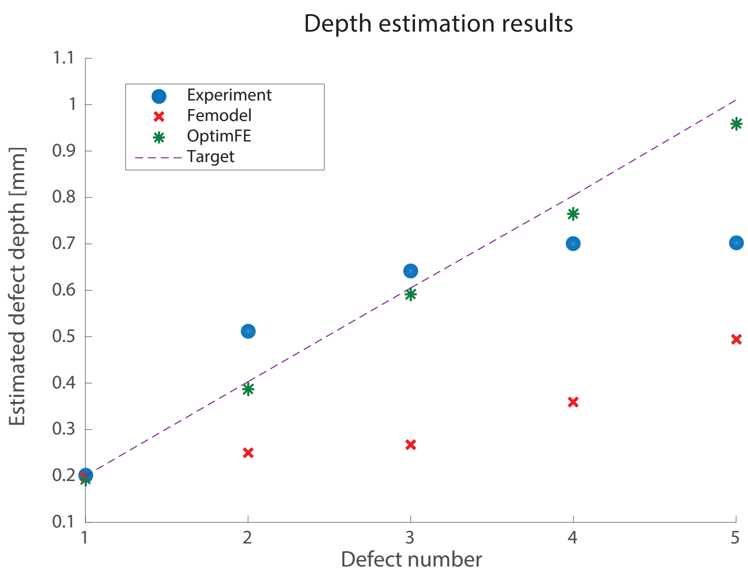

Figure 8: Depth estimation using standard pulsed thermography data on the CFRP test sample, the numerical model with standard material properties and the numerical model with optimised material properties.

2.3. Optimisation routine

The adaptive response surface optimisation routine is used to optimise numerical models with lots of data points and the time reducing by the algorithm increases as the number of parameters increases [14]. The routine is designed to handle multiple-output time series data [18]. The optimisation procedure can be divided into the following steps:

1. Starting reference simulation points is running and a correct object function is built of the difference between the FE model and the optimal target values defined in the objective function.
2. The FE model is replaced by a spline-based meta-model of response surfaces to decrease the optimisation time but remains an accurate approximation.
3. The optimisation routine is run on the specific object function to find the minimum for the meta-model. There is made use of an optimisation routine according to a genetic algorithm computation to find the optimum fast for the complex numerical model. Thereby the amount of FE solutions is further reduced.
4. The estimated parameter values are used as input parameters for an improved FE model that corrects the meta-model.
5. Only the points closer to the minimum are used to form the response surface (pan & zoom function).

The response model which is optimised is not built from a pre-defined number of design experiments, but is adapted and refined during the optimisation routine by the pan and zoom command [18]. The method automatically calculates the parameter influence sensitivity and sequentially resolves multiple sets with first the major influencing parameters with fixed parameter values for the minor influencing parameters. Succeeding, the second parameter set is optimised and finally an influence check is performed for all parameter sets until the results converge.

2.3.1. Objective function declaration

For the optimisation of the line scan thermography system, the declaration of the objective function is essential and closely related to the optimised experimental parameters. The most important parameters that influence the efficiency and accuracy of the thermal line scanning are:

- Robot speed u along the scanning direction;
- Excitation power P;
- Distance between heat source and the test sample d.

These parameters have implicit dependencies on the following parameters, which results in the complex objective function declaration:

- Image acquisition rate;
- Field of View (FOV);

- Scanning path;
- Minimum defect resolution.

It should be noted that these parameter values are highly dependent on the material properties of the structure under inspection.

The FOV is used to determine for each time instance which part of the inspected structure is visible using basic optical formulation represented in Eq.(4), with D the perpendicular distance between the camera and the structure. The scanning time is computed and minimised using basic path planning in combination with the robot speed u. This is combined with the computation of the minimal and maximal time instances, each point should be visibly related to the depth estimation of a possible defect according to Eq. (5), where α is the thermal diffusivity (m^2/s), C_1 a constant equal to 1.8 [27], f_b the blind frequency (Hz) and μ the diffusivity length (m). Therefore, the structure is divided into layers, related to the effective material layers defects are located. Reported experimental values of the constant C_1 are: $C_1 = 1$ when using amplitude data [36], and in the range $1.5 < C_1 < 2$ [36, 37, 38, 39, 40, 41] when working with the phase. The value $C_1 = 1.8$ is typically adopted [37, 38] following the research work by Thomas et al., 1980 [42]. The phase is therefore of more interest in NDT than the amplitude, since it provides deeper probing capabilities than the amplitude. Thereby, the inspection routine is optimised for the material and structure thickness of the specific structure.

$$x = 2 \cdot D \cdot tan(\frac{HFOV}{2}) \tag{4}$$

$$z = C_1 \sqrt{\frac{\alpha}{\pi \cdot f_b}} = C_1 \cdot \mu \tag{5}$$

These preparing criteria are combined with the objective function in which the total scanning time is minimised and the relative temperature difference between sound area and possible defective area is maximised. An important limit in the objective function is the maximum surface temperature of the structure which is dependent on the inspected material and which can overrule the objective function value to ignore certain unsafe inspection configurations. For the CFRP test sample, the maximum allowed surface temperature on which the surface in the numerical model is exposed to, is set to 323K. By implementing this boundary condition in the optimisation routine, a precaution is implemented to keep the non-destructive intention of the inspection routine.

2.4. Probability of Detection

A Probability of Detection (POD) analysis is performed to receive an objective comparison between the optimised detection results and the results received by an experienced LST inspector and a randomly chosen parameter set. A discrete hit/miss response is used in accordance with the work of Duan et al. [21]. The data is organised in a way that a defect is either detected (hit = 1) or not (miss = 0). The defect characterization is performed in relation to the aspect ratio using the log-odd model and a linear least square weighted special maximum likelihood method to estimate the model parameters [21]. The experimental and numerical results are first post-processed using Principal Component Thermography (PCT) to improve the defect detection capabilities [43, 21]. In relation to the work of Duan et al., there is used a region surrounding, but not containing, each defect as sound area. The size of the sound area is chosen in relation to the inspected defect with an equal surface. This comparison is used to perform an objective evaluation of the hit/miss criteria.

3. Results & Discussion

In the following section, the results of the optimisation routine are compared with the set-up parameters defined by an expert in dynamic line scan thermography and several iterative defined set-up parameter sets. The optimisation routine is validated on three different datasets performed on the CFRP006 sample. A representation of the Detected inserts after PCT post-processing is shown in Figure 9 for the shallow test sample. All parameter sets are described by:

1. D = perpendicular distance between the test sample and the heat source (mm);
2. u = speed of the robot arm (m/s);
3. P = power of the heat source (%) of 1500W;
4. d = horizontal distance between the camera and the heat source (mm).

The parameter set which is defined by the expert and the final parameter set after the optimisation routine are noted in the following figures.

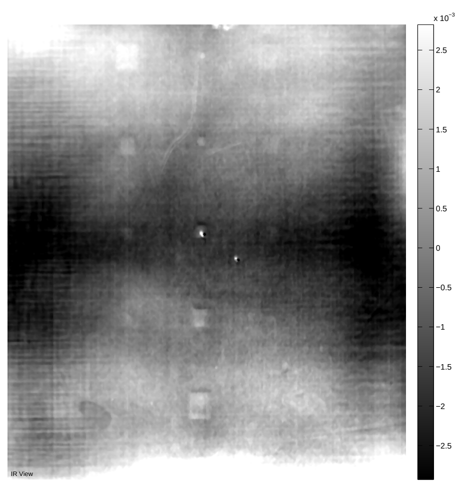

Figure 9: Detected teflon inserts in the shallow side of the testsample after Principal Component analysis.

3.1. Shallow side

The shallow side was analysed two times, one time for the data without adding extra noise and one time with extra noise added. Due to the very shallow defects of 0.2-1mm, the defect ratio is higher than 84%. As a result of the high detection ratio, the fitting of the POD curves is not consistent and the interpretation of these data sets is not applicable. One of the risks is a misinterpretation of the results as shown in Figure 10. It is shown in Figure 10b that the raw data should deliver a more accurate POD than the post-processed PCT data, which is in contrast to the findings of Duan et al. [21]. This is the reason that explains why it is important to use datasets with enough miss and hit data [44].

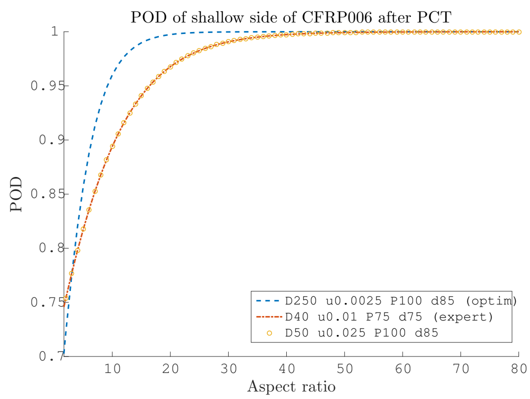

(a) Comparison of the Probability of detection for all parameter sets of the shallow test case after implementing PCT detection enhancement.

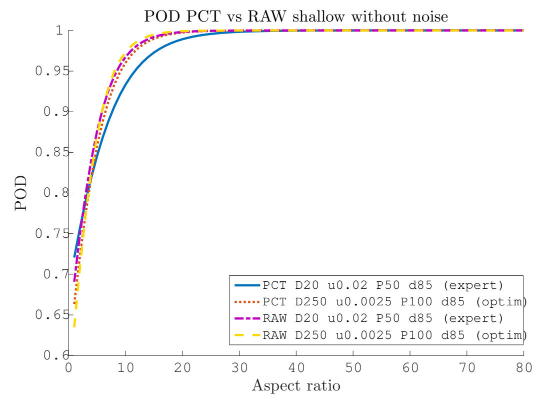

(b) Comparison of the Probability of Detection between the raw measurements and after post processing for both optimisation as expert parameter sets.

Figure 10: Analysis of shallow side of CFRP006 without noise adding. The legend is described in front of section 3.

3.2. Shallow side with noise

To use the shallow data set and to optimise the set-up for shallow structures it is essential to increase the amount of miss data to provide impossible to detect defects. It was chosen to do this by adding Gaussian noise to the camera data set. In this way, a camera is simulated with a higher NETD value. After the addition of the Gaussian noise, there are multiple defects that are impossible to detect and while some others are visible in all cases. A Gaussian distribution was chosen in order to avoid influence between the comparison of the RAW and PCT processed data. The results of the POD analysis are shown in Figure 11.

After adding the noise it is shown in Figure 11a that both the expert and the optimised results deliver similar POD curves and the differences for shallow defects are rather small. A major remark with these results is that due to the high distance D of the optimised results, it is possible to scan the object in one pass in contrast to the very low D of the expert set-up. This results in a lower scanning time and an easier scanning path of the

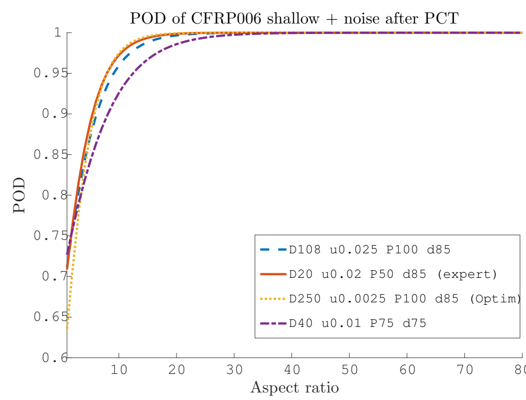

(a) Comparison of the Probability of detection for the shallow test case after adding Gaussian noise after implementing PCT detection enhancement.

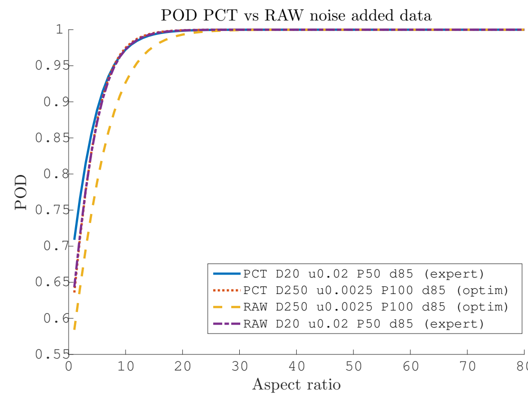

(b) Comparison of the Probability of Detection between the raw measurements and after post processing after adding Gaussian noise.

Figure 11: PoD analysis of shallow side of CFRP006 with Gaussian noise added.

optimised results in contrast to the path of the expert set-up which needs three passes. The implementation of PCT post-processing gives a major improvement, especially for the parameter sets with a higher D distance, which results on a lower spatial resolution. By post-processing the RAW measurements with PCT, the contrast is improved and the effect of smaller spatial resolution is reduced [43].

3.3. Comparison Shallow side with traditional active thermography

To verify the relevance of the performed measurements, a comparison is made with measurements performed by Duan et al. [21] on the same test sample. Within their setup, data acquisition was carried out using a Focal Plane Array (FPA) infrared camera (Santa Barbara Focalplane SBF125, 3 to 5 μm) with a 320×256 pixels array [21]. Besides, two high-power flashes (Balcar FX 60), each giving 3.2 kJ for 5 ms pulse duration, were used as heating sources in reflection mode [21]. The benchmark should be made on POD level and not on spatial quality of the measurement as there is made use of different equipment with different NETD levels and spatial resolution. An overview of the comparison is showed in Figure 12. The differences are limited and in advantage of the optimised LST measurements. It can be concluded that the measurements are performed adequate with respect to the state-of-the-art.

3.4. Deep side

The deep side has simulated defects between 1 and 1.8mm as described in section 2.1. The POD analysis is plotted versus the Aspect ratio which gives the relation to the size/depth ratio. Due to the depth and difficulty to detect the Teflon inserts on larger depths ($> 1mm$), the detection rate is less than 28%. The different set-up variations are compared after PCT post-processing in Figure 13. It is shown that both the expert set and

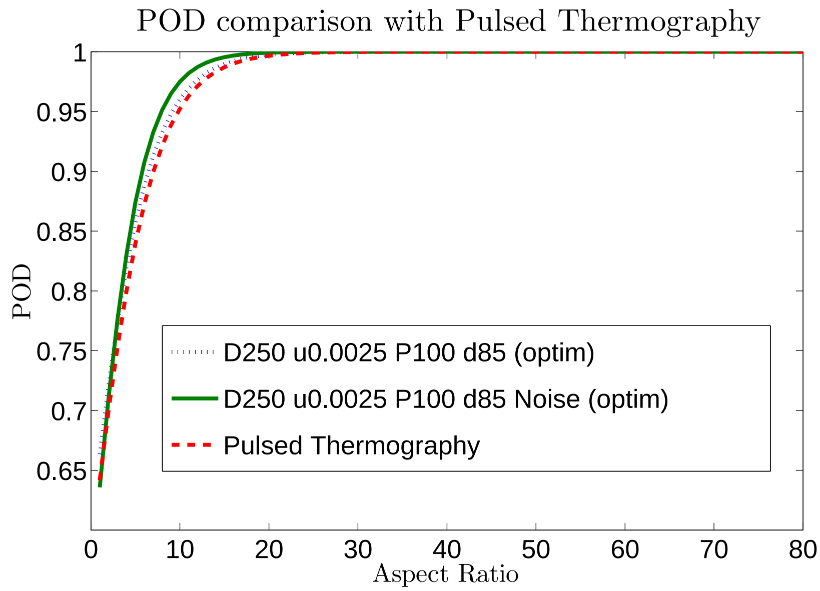

Figure 12: Probability of Detection for the shallow defect cases and standard pulsed thermography after PCT post-processing. The legend is described in front of section 3.

the optimised set of parameters deliver the best results, compared with the other parameter sets which are the result of a manual iterative process using trial and error. The optimised set is slightly better than the expert set and it should be remarked that by coincidence there is found a different parameter set during the iterative process which gives almost the same accuracy (D50). An important benefit of the optimised result is the consideration of scanning time. The higher the D distance, the fewer passes there are necessary and the faster the inspection could be performed. For this reason, the D160 set of parameters is preferred by the optimisation routine over the D50 set.

It should be pointed out that the optimised distance between the sample and the source D is smaller than the one required for the shallow side of the test sample. This is a logical and expected result considering that a smaller D implies that more energy is delivered to the surface, and as a consequence, deeper probing is possible.

At the same time, the optimisation algorithm proposed a scanning speed u much higher for the deep side as the decrease in D compensates for the loss of energy that a faster scanning would imply. In this way it is made possible to define a suitable set of inspection parameters necessary to detect defects of the individual structure.

3.5. Shallow versus Deep side

An interesting validation can be performed by comparing the overlapping defects at a depth of 1mm between the shallow and deep measurements. In Figure 14 both the POD curves and the binary detection rates are plotted. The POD curves are build from the combined measurements but exclusively from the data of the 1mm defects. The binary hit-miss data is split in the two different measurements. The Deep side of the testsample is represented by circles and the Shallow side by crosses. It can clearly be seen that the

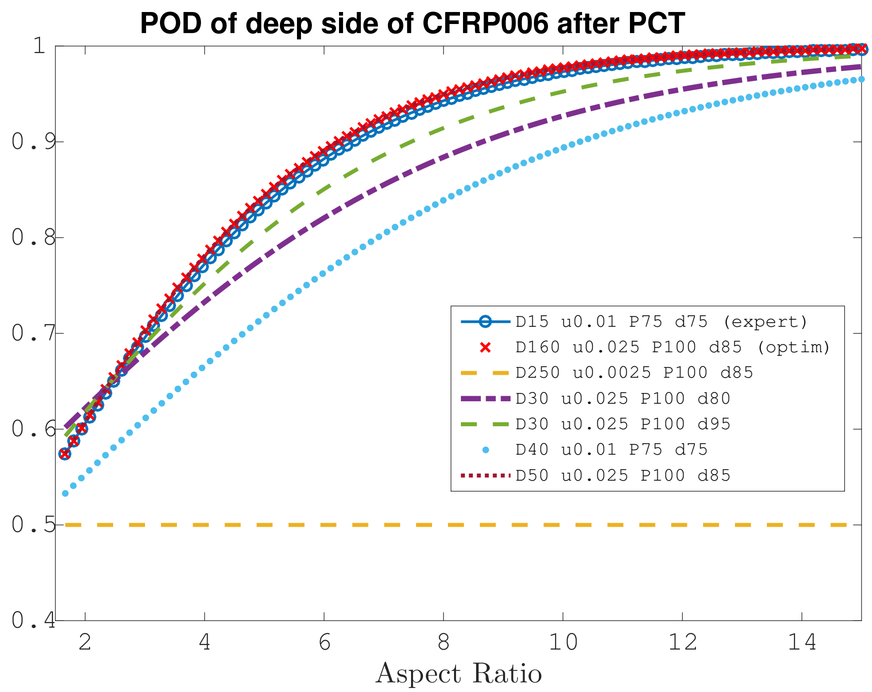

Figure 13: Probability of Detection for the deeper defect case on the CFRP006 sample after PCT post-processing. The legend is described in front of section 3.

results are equal for all aspect ratios except the one where the binary results flip from zero to one as can be seen in Figure 14. For the D40 case, the defect with aspect ratio 5 is not visible in contrast with the other parameter sets. A reasonable explanation can be found in the flipping point at this aspect ratio from not visible below aspect ratio 5 to visible above this aspect ratio and uncertainty due to measurement noise. The overlapping data of the testcase on a distance D equal to 250mm is neglected in Figure 14 as for both sides 0 defects are found in this dataset. Thereby we can conclude that the data is consistent for the overlapping setups between the two different sides.

4. Conclusions

The use of FE updating techniques can provide dynamic line scan set-ups with similar accuracy as set-up by an active thermography expert, with the added value that it automatically considers scanning time and path planning. The proposed method searches for the best possible measurement configuration to find the most defects in the specific structure. So if the range of depths is very broad, it will search for an optimum on which the shallow defects are still visible, the surface temperature is not to high and the deeper defects are starting to occur. In this way, it can be possible to efficiently modify NDE set-ups to inspect different serial produced complex parts and validate their accuracy using POD analysis. In longer term, the implementation of FE model updating in active thermography set-ups can support thermographers in choosing the most efficient measuring set-up for complex

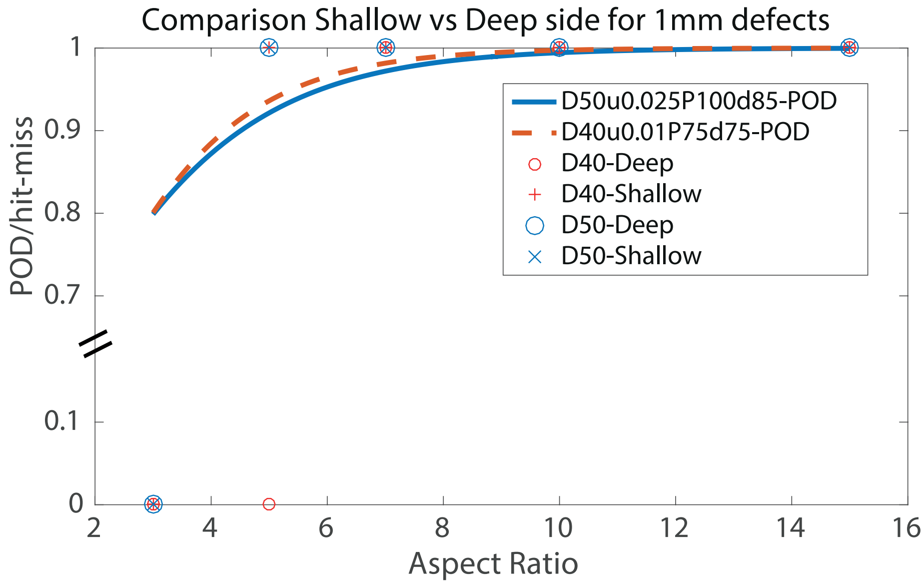

Figure 14: Comparison of 1mm defects measured from both sides.

shaped surfaces made of multiple materials. In this work an important keystone is provided which shows the implementation for shallow and deeper hard to detect Teflon inserts in a CFRP laminate. The results are validated on a flat surface. Continuing research will be performed to further improve the technology to implement directional emissivities.

Acknowledgements

The research leading to these results has received main funding from The Research Fund - Flanders FWO travel grant V4.010.16N and the University of Antwerp. The authors also acknowledge the Flemish government (GOA-Optimech) and the research council of the University of Antwerp (fti-OZC) for its funding. Furthermore the authors want to thank the support of the Canada Research Chair in Multipolar Infrared Vision (MIVIM) for supporting this research. We acknowledge also the support of the Natural Sciences and Engineering Research Council of Canada. At last the authors would like to thank the colleagues of the Op3Mech (B) and LVSN (CA) laboratories for their help.

Bibliography

[1] X. Maldague, Theory and practice of infrared thermography for nondestructive testing, Wiley, New York, 2001.
URL `http://scholar.google.com/scholar?hl=en&btnG=Search&q=intitle:theory+and+practic`

[2] M. Vollmer, K. Möllmann, Infrared thermal imaging: fundamentals, research and applications, Wiley-VCH, Berlin, 2010.
URL `http://books.google.com/books?hl=en&lr=&id=5SSiZAMwxtYC&oi=fnd&pg=PR15&dq=Infrar`

[3] N. Avdelidis, D. Almond, A. Dobbinson, B. Hawtin, Pulsed thermography : philosophy , qualitative and quantitative analysis on certain aircraft applications, in: Insight, Vol. 48, 2006, pp. 286–289.

[4] J. Peeters, B. Ribbens, J. J. J. Dirckx, G. Steenackers, Determining directional emissivity : Numerical estimation and experimental validation by using infrared thermography, Infrared Physics & Technologydoi:10.1016/j.infrared.2016.06.016.

[5] J. Hoshimiya, T. Hoshimiya, Whole-electronic line-focus light-scanner for active thermography, in: QIRT2014 Conférence, 2014, pp. 1–6.

[6] C. Ibarra-Castanedo, P. Servais, A. Ziadi, M. Klein, X. Maldague, RITA - Robotized Inspection by Thermography and Advanced processing for the inspection of aeronautical components camera heating source actuator camera heating, in: QIRT2014 Conférence, 2014, pp. 1–8.

[7] T. Schmidt, S. Dutta, T. Ullmann, Quantitative InfraRed Thermography Production integrated NDT by means of automated Thermography, International Conference on Quantitative Infrared Thermography (2012) 10.

[8] K. E. Cramer, W. P. Winfree, Thermographic detection and quantitative characterization of corrosion by application of thermal line source, Proceedings of SPIE - The International Society for Optical Engineering 3361 (1998) 291–300. doi:10.1117/12.304740.
URL `https://www.scopus.com/inward/record.uri?eid=2-s2.0-0032403325&partnerID=40&md5=`

[9] X. P. V. Maldague, Nondestructive Evaluation of Materials by Infrared Thermography, Springer London, London, 1993. arXiv:arXiv:1011.1669v3, doi:10.1007/978-1-4471-1995-1.
URL `https://books.google.be/books?id=6MHcBwAAQBAJ` `http://link.springer.com/10.1007/978-1-4471-1995-1`

[10] P. Lindberg, A Prism Line-scanner for High-speed Thermography, Optica Acta: International Journal of Optics 15 (4) (1968) 305–316. doi:10.1080/713818101.
URL `http://www.tandfonline.com/doi/abs/10.1080/713818101`

[11] Mistras, MIstras Line Scan thermography: necessary in industry (2012).
URL `https://spinoff.nasa.gov/Spinoff2012/ip_4.html`

[12] D. F. Woolard, K. E. Cramer, The thermal photocopier: a new concept for thermal NDT, in: SPIE, Vol. 5405, 2004, p. 366. doi:10.1117/12.541881.
URL `http://proceedings.spiedigitallibrary.org/proceeding.aspx?doi=10.1117/12.541881`

[13] O. Ley, V. Godinez-Azcuaga, Line Scanning Thermography and its Application Inspecting Aerospace Composites, in: 5th International Symposium on NDT in Aerospace, 2013, pp. 13–15.
URL `http://www.ndt.net/article/aero2013/content/papers/48_Godinez-Azcuaga.pdf`

[14] G. Steenackers, P. Guillaume, Finite element model updating taking into account the uncertainty on the modal parameters estimates, Journal of Sound and Vibration 296 (4-5) (2006) 919–934. doi:10.1016/j.jsv.2006.03.023.
URL `http://linkinghub.elsevier.com/retrieve/pii/S0022460X06002719`

[15] M. Meo, G. Zumpano, Damage assessment on plate-like structures using a global-local optimization approach, Optimization and Engineering 9 (2) (2008) 161–177. doi:10.1007/s11081-007-9016-0.

[16] J. Mottershead, M. Friswell, Model Updating In Structural Dynamics: A Survey (1993). doi:10.1006/jsvi.1993.1340.
URL `http://www.sciencedirect.com/science/article/pii/S0022460X83713404`

[17] H.-C. Cheng, Y.-H. Tsai, K.-N. Chen, J. Fang, Thermal placement optimization of multichip modules using a sequential metamodeling-based optimization approach, Applied Thermal Engineering 30 (17-18) (2010) 2632–2642. doi:10.1016/j.applthermaleng.2010.07.004.
URL `http://linkinghub.elsevier.com/retrieve/pii/S1359431110002875`

[18] J. Peeters, G. Arroud, B. Ribbens, J. Dirckx, G. Steenackers, Updating a finite element model to the real experimental setup by thermographic measurements and adaptive regression optimization, Mechanical Systems and Signal Processing 64-65 (2015) 428–440. doi:10.1016/j.ymssp.2015.04.010.
URL `http://linkinghub.elsevier.com/retrieve/pii/S0888327015001697`

[19] T. Marwala, Finite-element-model Updating Using Computational Intelligence Techniques, Springer, 2010.
URL `http://books.google.com/books?id=ObtwUF1uAqMC&pgis=1`

[20] R. K. Nagle, E. B. Saff, A. D. Snider, Fundamentals of Differential Equations and Boundary Value Problems, Pearson education, 2012.

[21] Y. Duan, P. Servais, M. Genest, C. Ibarra-Castanedo, X. P. V. Maldague, ThermoPoD: A reliability study on active infrared thermography for the inspection of composite materials, Journal of Mechanical Science and Technology 26 (7) (2012) 1985–1991. doi:10.1007/s12206-012-0510-8.

[22] A. J. Hodge, J. L. Walker, Probability of Detection Study on Impact Damage To Honeycomb Composite Structure Using Thermographic Inspection, in: Proc. 40th International SAMPE Technical Conference (ISTC), Memphis, 2008.

[23] J. DiMambro, K. A. Rackow, D. P. Roach, S. M. Shepard, T. Ahmed, A Composite Honeycomb Probability of Detection (POD) Experiment using an Uncooled Infrared Camera for Pulsed Thermography, in: 49th Annual Air Transport Association (ATA) NDT Forum, Ft. Worth North, TX, USA, 2006.

[24] J. DiMambro, Quantitative evaluation of emerging infrared thermography technologies for aerospace applications, in: C. H. Chen (Ed.), Ultrasonic and Advanced Methods for Nondestructive Testing and Material Characterization, World Scientific, 2007, Ch. 15.

[25] Y. Guo, F. R. Ruhge, Comparison of detection capability for acoustic thermography, visual inspection and fluorescent penetrant inspection on gas turbine components, in: AIP Conference Proceedings, Vol. 1096, 2009, pp. 1848–1854. doi:10.1063/1.3114183.

[26] E. Ginzel, Introduction to the Statistics of NDT, NDT.net 11 (5) (2006) 1.
URL `http://www.ndt.net/article/v11n05/ginzel2/ginzel2.htm`

[27] C. Ibarra-Castanedo, X. P. V. Maldague, Interactive methodology for optimized defect characterization by quantitative pulsed phase thermography, Research in Nondestructive Evaluation 16 (4) (2005) 175–193. doi:10.1080/09349840500351846.

[28] F. Lopez, C. Ibarra-Castanedo, V. de Paulo Nicolau, X. Maldague, Optimization of pulsed thermography inspection by partial least-squares regression, NDT & E International 66 (2014) 128–138. doi:10.1016/j.ndteint.2014.06.003.
URL `http://linkinghub.elsevier.com/retrieve/pii/S0963869514000760`

[29] P. Brown, A. Hindmarsh, L. Petzold, Using Krylov Methods in the Solution of Large-Scale Differential-Algebraic Systems, SIAM Journal Scientific Computing 15 (1994) 1467–1488.

[30] A. J. Chapman, Heat transfer, 4th Edition, Macmillan, New York, 1984.

[31] B. Stotter, K. Gresslehner, G. Mayr, G. Hendorfer, J. Sekelja, Quantitative application of pulse phase thermography to determine material parameters, in: Quantitative infrared thermography(Qirt)-Bordeaux, Bordeaux, 2014, p. 10.
URL `http://qirt.org/archives/qirt2014/QIRT 2014 Papers/QIRT-2014-074.pdf`

[32] (Comsol Multiphysics), Comsol Documentation (2015).

[33] Granta Design Limited, CES Edupack 2013 (2013).

[34] R. Joven, R. Das, A. Ahmed, P. Roozbehjavan, B. Minaie, Thermal properties of carbon fiber epoxy composites with different fabric weaves, in: SAMPE International Symposium Proceedings, 2012, p. 14.

[35] J. Peeters, C. Ibarra-Castanedo, S. Sfarra, X. Maldague, J. Dirckx, G. Steenackers, Robust Quantitative Depth Estimation on CFRP samples using active thermography inspection and numerical simulation updating, NDT & E International-doi:10.1016/j.ndteint.2017.02.003.
URL `http://linkinghub.elsevier.com/retrieve/pii/S0963869517300920`

[36] G. Busse, A. Rosencwaig, Subsurface imaging with photoacoustics, Applied Physics Letters 36 (10) (1980) 815–816. doi:10.1063/1.91327.

[37] C. Meola, G. M. Carlomagno, L. Giorleo, The use of infrared thermography for materials characterization, J. Mater. Process. Technol. 155 (2004) 1132–1137.

[38] C. Meola, G. M. Carlomagno, Recent advances in the use of infrared thermography, Measurement Science and Technology 15 (9) (2004) R27–R58. doi:10.1088/0957-0233/15/9/R01.

[39] W. Bai, B. S. Wong, Evaluation of defects in composite plates under convective environments using lock-in thermography (2001). doi:10.1088/0957-0233/12/2/303.

[40] G. Busse, Nondestructive evaluation of polymer materials, NDT & E International 27 (5) (1994) 253–262. doi:10.1016/0963-8695(94)90130-9.
URL `http://linkinghub.elsevier.com/retrieve/pii/0963869594901309`

[41] C. Ibarra-castanedo, Quantative subsurface defect evaluation by Pulsed Phase Thermography, Ph.D. thesis (2005).

[42] R. L. Thomas, J. J. Pouch, Y. H. Wong, L. D. Favro, P. K. Kuo, A. Rosencwaig, Subsurface flaw detection in metals by photoacoustic microscopya, Journal of Applied Physics 51 (2) (1980) 1152–1156.

[43] N. Rajic, Principal component thermography, defense science and techno.
URL `http://oai.dtic.mil/oai/oai?verb=getRecord&metadataPrefix=html&identifier=ADA405`

[44] US Air force Aeronautical Systems Center, Non-destructive Evaluation System Reliability Assessment, Military Handbook, 2009.